RSC Advances

PAPER

View Article Online
View Journal | View Issue

Cite this: *RSC Adv.*, 2017, 7, 50006

Heterostructured $ZnFe_2O_4/TiO_2$ nanocomposites with a highly recyclable visible-light-response for bisphenol A degradation†

Thanh Binh Nguyen[a] and Ruey-an Doong*[ab]

Novel visible-light-sensitive $ZnFe_2O_4$–TiO_2 heterojunction photocatalysts are successfully fabricated by a facile solvothermal method for the enhanced photocatalytic degradation of bisphenol A (BPA) under different light sources. The photocatalytic degradation efficiency and rate of BPA by $ZnFe_2O_4$–TiO_2 under the irradiation of different light sources follow the order 465 nm visible light > solar simulator > 365 nm UV light. The reaction rate of BPA by $ZnFe_2O_4$–TiO_2 in the presence of 465 nm visible light is 42 times higher than that under 365 nm UV light irradiation. In addition, the $ZnFe_2O_4$–TiO_2 nanocomposites exhibit excellent recycling and reusability and can retain their stable photocatalytic activity toward BPA photodegradation for at least 10 cycles of reaction with rate constants of 0.191–0.218 min^{-1} under visible light irradiation. The photogenerated holes as well as oxygen-containing radicals are identified to be the predominant reactive species responsible for the photodegradation of BPA in the $ZnFe_2O_4$–TiO_2 system. The possible reaction mechanisms for BPA photodegradation by p–n heterojunction $ZnFe_2O_4$–TiO_2 are also proposed. Results obtained in this study clearly demonstrate the superior visible-light-driven photoactivity of $ZnFe_2O_4$–TiO_2 toward BPA photodegradation and can open an avenue to fabrication of p–n heterojunctions of photocatalysts with a wide variety of potential applications in the fields of photocatalysis, water splitting and energy conversion.

Received 27th July 2017
Accepted 20th October 2017

DOI: 10.1039/c7ra08271a

rsc.li/rsc-advances

1. Introduction

The development of highly efficient visible-light-driven photocatalysts for energy and environmental applications has recently attracted much attention. Titanium-based nanomaterials such as titanium dioxide (TiO_2) nanoparticles have long been used as the photocatalysts for a wide variety of applications including water splitting, dye-sensitized solar cells (DSSCs), and photocatalytic degradation of emerging pollutants.[1–4] In addition, various morphologies of titanium-based nanomaterials including 1-dimensional TiO_2 nanotube arrays, titanate nanotubes and hollow TiO_2 nanomaterials have been developed for the enhancement of photocatalytic efficiency on water splitting and photodegradation of pollutants.[5–8] However, these materials still suffer the limitation of efficient utilization of visible light. Therefore, the development of novel visible-light-driven photocatalysts which can effectively utilize visible and solar lights is urgently needed.

More recently, a particular interest in the development of visible-light-responsive photocatalysts is the synthesis of nanocrystalline spinel ferrite. Spinel ferrites including $NiFe_2O_4$, $ZnFe_2O_4$ and $CuFe_2O_4$ have possessed unique photocatalytic properties for the removal of inorganic contaminants,[9–11] antimicrobial activity[12] and organic dyes.[13–17] In addition, the spinel crystal structure of ferrites offers the available extra catalytic sites by virtue of the crystal lattices and a band gap capable of absorbing visible light to enhance the photodegradation efficiency of pollutants.[18] Among the spinel structured materials used, $ZnFe_2O_4$ is a magnetic material with a relatively narrow bandgap of 1.9 eV which has attracted considerable attention on the conversion of solar energy, water splitting and DSSC.[19–23] However, the low valence band potential and poor photoelectric conversion efficiency makes $ZnFe_2O_4$ an inferior photocatalyst toward pollutants degradation.[24,25] Previous studies have shown that the coupling of $ZnFe_2O_4$ with optoelectronic materials such as TiO_2, ZnO and graphene can form a new type of nanocomposite with good photocatalytic activity.[26–28] It is noteworthy that $ZnFe_2O_4$ is a p-type visible-light-driven semiconductor, while anatase TiO_2 is a well-known n-type semiconductor with indirect bandgap and long electron–hole life time.[29,30] The combination of $ZnFe_2O_4$ and TiO_2 with p–n heterojunction can thus extend the absorption to the visible light region. Our previous study has depicted that $ZnFe_2O_4$–TiO_2 heterostructures can effectively photodegrade of organic dyes

---

[a] Department of Biomedical Engineering and Environmental Sciences, National Tsing Hua University, Hsinchu, 30013, Taiwan. E-mail: radoong@mx.nthu.edu.tw

[b] Institute of Environmental Engineering, National Chiao Tung University, Hsinchu, 30010, Taiwan. E-mail: radoong@nctu.edu.tw

† Electronic supplementary information (ESI) available: Photoluminescence spectra; FT-IR spectra of octanol; the photodegradation of bisphenol A by as-prepared $ZnFe_2O_4$, ST-01 TiO_2, and P25 TiO_2; EDS. See DOI: 10.1039/c7ra08271a

including rhodamine B and methylene orange under visible light irradiation.[31] This means that the $ZnFe_2O_4$–TiO_2 nanocomposite may be a good photocatalyst capable of photodegradation of a wide variety of environmental contaminants. However, very little information is available regarding the photocatalytic activity of $ZnFe_2O_4$–TiO_2 nanocomposites toward emerging pollutants degradation under visible light irradiation.

The contamination of emerging pollutants such as pharmaceuticals and endocrine disrupting chemicals in water and wastewater have been becoming a globally concerning issue. Bisphenol A (BPA), one of the representative emerging pollutants, has been widely used for the manufacture of numerous products of epoxy resins and polycarbonate plastics utilized in a wide variety of food and drinking packaging applications.[32–35] BPA can be easily released to the environment and get into human body through the discharge of domestic sewages and industrial wastewater as well as the plastic products such as baby bottles and food packages. Since BPA has estrogenically toxic risk to human beings, the searching of effective detoxification technology is thus urgently needed. Several studies have developed the metal ion-doped photocatalysts to degrade BPA in water and wastewater.[36,37] However, the photocatalytic activity of $ZnFe_2O_4$–TiO_2 toward BPA degradation in the presence of different light sources such as UV light, visible light and solar simulator has received less attention. In addition, the photodegradation kinetics as well as the possible reaction mechanisms for BPA photodegradation by $ZnFe_2O_4$–TiO_2 remains unclear.

Herein, the $ZnFe_2O_4$–TiO_2 heterojunction nanophotocatalysts were fabricated by a facile solvothermal method for the enhanced photocatalytic degradation of BPA under different light sources with various wavelength ranges. Three different lamps including 365 nm UV light, 465 ± 40 nm visible light and solar simulator at AM 1.5 were selected as the light sources to elucidate the visible-light-driven photocatalytic activity of $ZnFe_2O_4$–TiO_2. In addition, the stability and reusability of $ZnFe_2O_4$–TiO_2 was evaluated under visible light irradiations. Results show that the $ZnFe_2O_4$–TiO_2 can generate large amounts of oxygen-containing radicals for BPA photodegradation under the irradiation of both 465 nm visible light and solar simulator, while the high e^-–h^+ recombination rate and photo-lability of $ZnFe_2O_4$ at 365 nm UV light lower the photocatalytic efficiency and rate of BPA. To the best of our knowledge, this is the first report to elucidate the effect of different light sources on the photocatalytic activity of $ZnFe_2O_4$–TiO_2 heterojunctions and the photocatalytic activity of $ZnFe_2O_4$–TiO_2 toward BPA degradation in the presence of 465 nm visible light is superior to that of 365 nm UV light. In addition, the contribution of radical species produced from the irradiation of $ZnFe_2O_4$–TiO_2 with visible light is determined and the possible reaction mechanism for BPA photodegradation by $ZnFe_2O_4$–TiO_2 is proposed. Results obtained in this study clearly demonstrate the excellent visible-light-driven photocatalytic activity of $ZnFe_2O_4$–TiO_2 and can pave the gateway to fabricate p–n heterojunction photocatalysts for the decomposition of emerging pollutants, water splitting and energy conversion in the presence of visible light.

2. Experimental

2.1. Fabrication of $ZnFe_2O_4$–TiO_2 nanocomposites

Zinc ferrite nanoparticles were synthesized by non-aqueous hydrothermal method by dissolving 0.5 mmol of oleic acid ($C_{18}H_{34}O_2$) and 0.5 mmol oleylamine ($C_{18}H_{37}N$) into the mixture containing 10 mL of 1-pentanol ($C_5H_{12}O$) and 2 mL of 5 M NaOH solution.[31] Iron nitrate ($Fe(NO_3)_3 \cdot 9H_2O$) and zinc nitrate ($Zn(NO_3)_2 \cdot 6H_2O$) at molar ratio of 2 : 1 was dissolved in bidistilled deionized water (18.3 MΩ cm) and then was poured into the above solution under vigorous mixing for 1 h. The mixture was then heated to 180 °C for 16 h and cooled to room temperature. The $ZnFe_2O_4$ nanoparticles were magnetically harvested and washed with *n*-hexane/ethanol (3/1, v/v) mixture and then dried in a vacuum oven at 60 °C for 6 h.

$ZnFe_2O_4$–TiO_2 nanocomposites were synthesized by mixing 80 mg of ST01 TiO_2 (Ishihara Sangyo Ltd., Tokyo, Japan) with 1 wt% (0.808 mg) of $ZnFe_2O_4$ in 20 mL of octanol ($C_8H_{18}O$) and then dispersed in an ultrasonic bath for 1 h. The mixture was then heated and refluxed at 140 °C for 2 h under vigorous stirring conditions to improve the attachment of $ZnFe_2O_4$ on the surface of TiO_2 nanoparticles to form $ZnFe_2O_4$–TiO_2 heterojunction. After cooling to the room temperature, the products were harvested by centrifugation and washed with the mixture of *n*-hexane/ethanol for several times. The purified powders were dried in a vacuum oven at 60 °C for 6 h and stored in a desiccator for further use.

2.2. Characterization

The surface morphology of as-synthesized $ZnFe_2O_4$–TiO_2 was examined by using a scanning electronic microscope (SEM) (Hitachi S-4800) with an acceleration electron voltage of 15 kV. The dimension and morphology of $ZnFe_2O_4$–TiO_2 were obtained by the FEI tecnai G2 transmission electron microscope (TEM) with an energy-dispersive X-ray spectroscope (EDS) at an accelerating voltage of 200 kV. The crystallinity was identified by using a Bruker NEW D8 ADVANCE X-ray diffractometer (XRD) with a Lynxeye high-speed strip detector and Ni filtered Cu Kα radiation ($\lambda = 1.5405$ Å) operating at a generator voltage and an emission current of 40 kV and 40 mA, respectively. The XRD patterns were recorded over the 2θ range of 20–80° at a sampling step width 0.05° and a step time of 0.5 s. The optical property of $ZnFe_2O_4$–TiO_2 nanocomposites was examined by using a UV-visible spectrophotometer (Hitachi U-4100) equipped with the integrated sphere accessory. Photoluminescence (PL) spectra were recorded on a Hitachi F-7000 fluorescence spectrometer with a 150 W xenon lamp as the excitation source. FTIR spectra were obtained by a Horiba FT-720 spectrometer at a resolution of 2 cm^{-1} with KBr method. Thermogravimetric analysis (TGA) was performed using a TGA-DSC 3+ thermal analyzer (Mettler Toledo). The temperature increased from room temperature to 1000 °C at a heating rate of 10 °C min^{-1} under nitrogen atmosphere. Electrochemical impedance spectroscopy (EIS) was performed in a three-electrode system using an electrochemical work station (Autolab PGSTAT 302N) in a 0.2 M Na_2SO_4 aqueous solution and in a frequency range of 100 kHz to 100 mHZ. The working electrode was prepared by coating 2 mg of $ZnFe_2O_4$–TiO_2 nanocomposites dispersed in ethanol onto a 2 cm × 2 cm fluorine-tin oxide (FTO) glass electrode. The platinum wire and Ag/AgCl were used as the counter and reference electrodes, respectively.

2.3. Photocatalytic degradation of BPA by $ZnFe_2O_4$–TiO_2

The photocatalytic activity of as-prepared $ZnFe_2O_4$–TiO_2 nanocomposites toward BPA degradation was examined in a quartz reactor surrounded by eight 8 W visible light lamps ($\lambda = 465 \pm 40$ nm) or UV light lamps at 365 nm. For solar light experiments, an Oriel Class A solar simulator (Model no. 91160A) equipped with AM 1.5G filter (Model no. 81088A) and a 300 W xenon lamp (Model no. 6258) was used as the light source, and was calibrated by using a reference Si reference solar cell (NREL Institutes, USA). For each experiment, 1 g L^{-1} as-synthesized $ZnFe_2O_4$–TiO_2 photocatalysts was added into the 20 mL of solutions containing 10 mg L^{-1} BPA at pH 7. In addition, the photocatalytic degradation of BPA by commercial TiO_2 nanoparticles including P-25 and ST-01 TiO_2 was performed under the same conditions for comparison. The experiments were carried out in the dark and under the irradiation of different light sources with the same light intensity of 150 mW cm^{-2} by adjusting the exposed surface area of the quartz reactor to maintain a consistent irradiation effect. The numbers of photon hitting the solution in the photocatalytic reactor are 0.9×10^{19}, 1.1×10^{19}, and 1.2×10^{19} photons per second for UV (365 nm), visible (465 nm), and solar (major peak at 500 nm) lights, respectively.

Prior to the irradiation, the mixtures were well-mixed under vigorous stirring conditions in the dark for 60 min and at 25 °C to establish the adsorption equilibrium of BPA with photocatalysts. After the adsorption equilibrium, the light sources were switched on for photodegradation of BPA by various photocatalysts and aliquots (1 mL) was withdrawn from the solution at the selected time intervals. After liquid–solid separation through the centrifugation at 14 000 rpm for 5 min, the BPA concentration in aqueous solution was measured by using Agilent Technologies 1200 high performance liquid chromatograph (HPLC) equipped with photodiode array (PDA) as the detector. In addition, the C-18 column (LUNA 5u 100A, 4.6 mm × 250 mm, Phenomenex) with mobile phase of methanol/acetonitrile/water (50 : 30 : 20, v/v) solution at a flow rate of 0.5 mL min^{-1} was used to identify BPA. The BPA concentration was determined based on the absorbance at 225 nm. In addition, the photo-generated free radicals from the photodegradation of BPA by $ZnFe_2O_4$–TiO_2 in the presence of 4.4 mM 5,5-dimethyl-1-pyrroline *N*-oxide (DMPO) was examined in ethanol and aqueous solutions using an electron spin resonance (ESR) spectrometer (Bruker, EMX-10, Germany).

2.4. Reaction kinetics

It is well-established that the reaction of organic chemicals onto heterogeneous catalysts can be described by the Langmuir–Hinshelwood kinetic model. For photocatalytic degradation, BPA needs to adsorb onto the surface of $ZnFe_2O_4$–TiO_2 nanocomposites first, and then reacts with the reactive species on photocatalyst for photodegradation. Therefore, the Langmuir–Hinshelwood kinetic model can be used to describe the photocatalytic degradation of BPA by $ZnFe_2O_4$–TiO_2:

$$r_0 = \frac{\mathrm{d}C_\mathrm{R}}{\mathrm{d}t} = k_\mathrm{r}\frac{K_\mathrm{a}C_\mathrm{R}}{1 + K_\mathrm{a}C_\mathrm{R}} \tag{1}$$

where r_0 is the initial rate for BPA photodegradation, C_R is the BPA concentration, k_r is the intrinsic rate constant and K_a is the Langmuir coefficient of BPA. When $K_\mathrm{a}C_\mathrm{R}$ is small (<1), eqn (1) can be simplified to the pseudo-first-order kinetics:

$$\ln\left(\frac{C}{C_\mathrm{o}}\right) = -k_\mathrm{obs}t \tag{2}$$

where k_obs is the pseudo-first-order rate constant for BPA photodegradation (min^{-1}).

3. Results and discussion

3.1. Characterization of $ZnFe_2O_4$–TiO_2 nanocomposites

TEM images were first used to identify the morphology and structure of $ZnFe_2O_4$–TiO_2 nanocomposites. The TEM image shows that the $ZnFe_2O_4$–TiO_2 nanocomposites are regular-shaped nanoparticles (Fig. 1a). However, the $ZnFe_2O_4$–TiO_2 nanoparticles agglomerate to some extents, presumably attributed to the magnetic property of $ZnFe_2O_4$ particles. The coexistence of $ZnFe_2O_4$ and TiO_2 can be confirmed by HRTEM image. As shown in Fig. 1b, both $ZnFe_2O_4$ and ST-01 TiO_2 are nanosized particles with diameters of 7–10 nm. Two distinct lattice fringes with *d*-spacing of 0.25 and 0.35 nm, which can be ascribed to the (311) and (101) planes of $ZnFe_2O_4$ and anatase TiO_2, respectively, are observed. Moreover, an intimate interface between two nanoparticles is observed. This indicates that the heterojunction between p-type $ZnFe_2O_4$ and n-type TiO_2 can facilitate the charge transfer more readily to significantly reduce the recombination of electron–hole pairs as well as to enhance the visible-light-driven photocatalytic activity of $ZnFe_2O_4$–TiO_2 nanocomposites.

The XRD patterns shown in Fig. 1c clearly displays the anatase TiO_2 peaks at 25.41°, 38.05°, 48.03°, 54.30°, 54.94°, 62.80°, 68.74°, 70.07° and 75.28° 2θ. In addition, a small peak appeared at 35.29° 2θ is the characteristic peak of (311) plane of $ZnFe_2O_4$ nanoparticles, which is in good agreement with the results obtained from HRTEM image. It is noteworthy that only few XRD peaks of $ZnFe_2O_4$ is observed, presumably attributed to the low loaded amount of 1 wt% $ZnFe_2O_4$ onto TiO_2 surface. The EDS spectrum shown in Fig. 1d indicates the existence of Ti, Zn, Fe and O elements and the atomic ratio of Fe/Zn in the heterostructures (Fe/Zn = 2.1) is close to the theoretical molar ratio of 2 (Table S1, ESI†). Moreover, the mass loading of $ZnFe_2O_4$ is calculated to be 1.02 wt% from EDS spectra, clearly indicating that non-aqueous hydrothermal method can synthesize 1 wt% $ZnFe_2O_4$–TiO_2 nanocomposites. It is noteworthy that the weight ratio of each component in the $ZnFe_2O_4$–TiO_2 nanocomposites has a great influence on the photocatalytic activity of heterojunction. Our previous study has demonstrated that addition of 0.2–2 wt% $ZnFe_2O_4$ to TiO_2 nanoparticles can enhance the

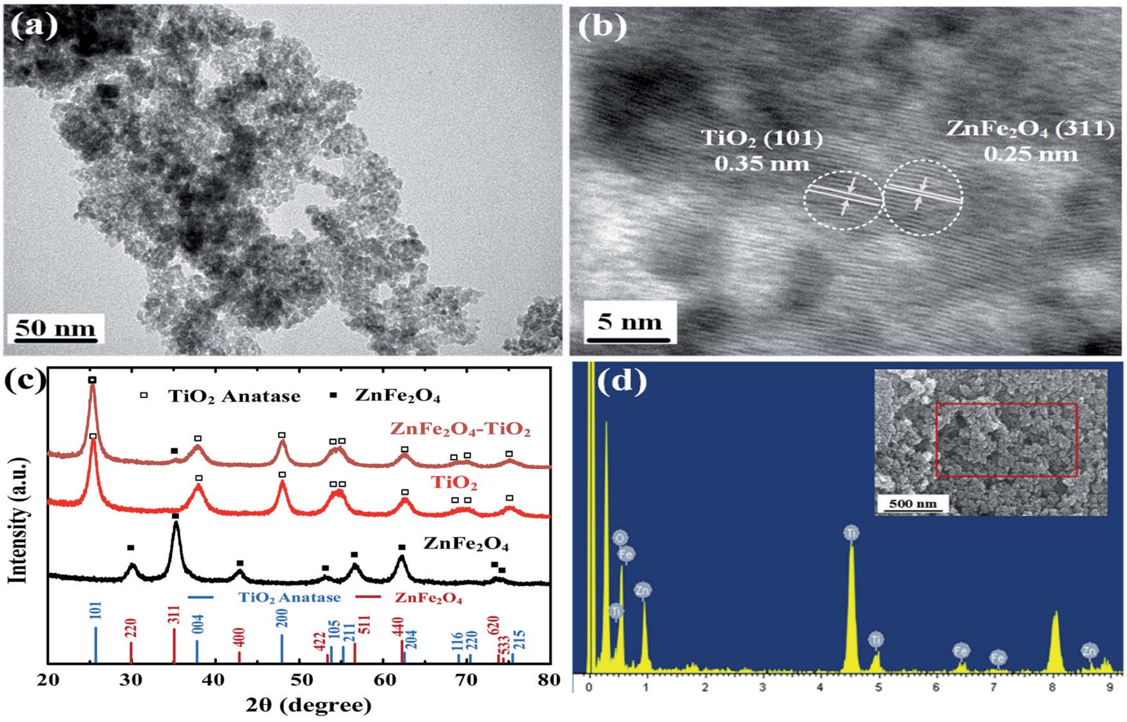

Fig. 1 (a) TEM and (b) HRTEM images, (c) XRD patterns and (d) EDS spectrum of $ZnFe_2O_4$–TiO_2 nanocomposites. The inset of (d) is the analytical area of SEM image for EDS.

photocatalytic degradation efficiency of organic dyes and the optimal added amount of $ZnFe_2O_4$ is 1 wt%.[31] Therefore, 1 wt% $ZnFe_2O_4$–TiO_2 was selected in this study for photodegradation of BPA under different light sources irradiation.

Fig. 2a shows the optical property of as-prepared $ZnFe_2O_4$–TiO_2 nanocatalysts. The absorption edges of pure ST01 TiO_2 and $ZnFe_2O_4$ starts at 380 and 550 nm, respectively, which are consistent with the reported data of anatase TiO_2 and $ZnFe_2O_4$.[31] The UV-visible spectra of 1 wt% $ZnFe_2O_4$–TiO_2 shows an absorption in the visible light region, which indicates that the extension of absorption edge to the visible light region is mainly attributed to the existence of $ZnFe_2O_4$. This extension

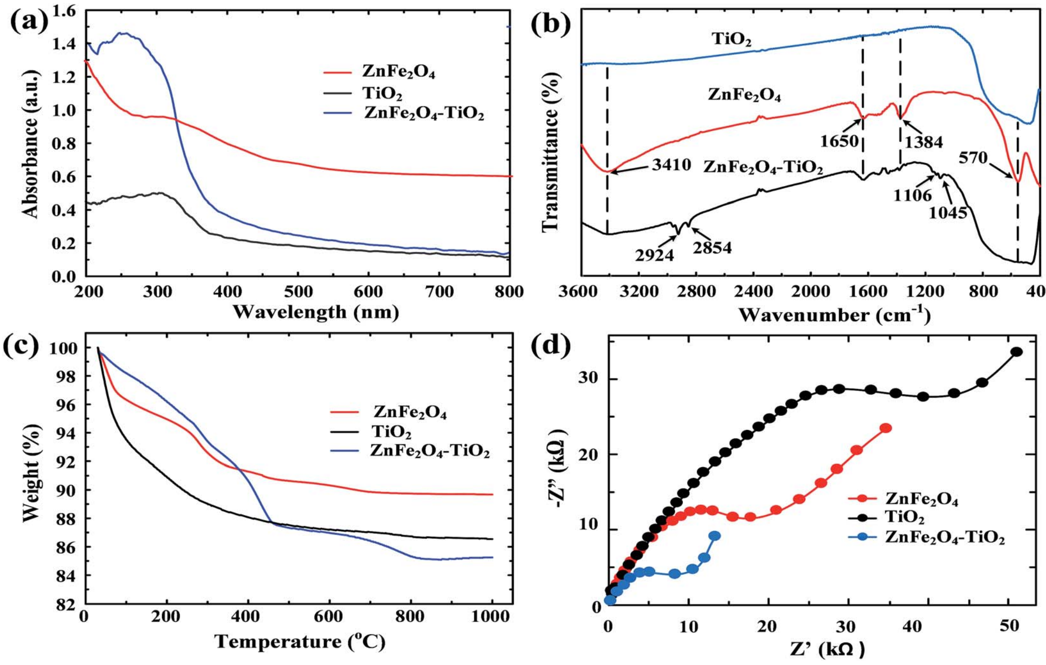

Fig. 2 The optical properties of (a) UV-visible and (b) FT-IR spectra, (c) TGA curve and (d) Nyquist plots of $ZnFe_2O_4$, TiO_2 and $ZnFe_2O_4$–TiO_2.

behavior depicts that $ZnFe_2O_4$–TiO_2 may contain more lattice defects in the nanocomposites, which can serve as the center of bound excitons to drive the separation and transportation of photogenerated electron–hole pairs.[38]

The retardation of electron–hole recombination is optically examined. Fig. S1 (ESI†) shows the photoluminescence spectra of commercial TiO_2, as-prepared $ZnFe_2O_4$ and 1 wt% $ZnFe_2O_4$–TiO_2 nanocomposite after the irradiation of excitation wavelength at 285 nm. The photoluminescence spectra of all the nanomaterials show a major peak at 315 nm, which is the characteristic peak of the recombination of hole and electron in the valence and conduction bands, respectively. The decrease in photoluminescence intensity of 1 wt% $ZnFe_2O_4$–TiO_2 nanocomposite indicates the obvious retardation of electrons and holes, which is in good agreement with our previous result.[31] This means the successful fabrication of p–n $ZnFe_2O_4$–TiO_2 heterojunction, which can be used for visible-light-sensitive photodegradation.

The FTIR spectrum of TiO_2 shows a broad band at 455 cm^{-1}, which can be assigned as the Ti–O–Ti stretching mode (Fig. 2b). Two inherent stretching vibration of M–O bonds centering at 570 cm^{-1} (Fe–O) and 400 cm^{-1} (Zn–O) appear in the as-prepared $ZnFe_2O_4$ spectrum, confirming the spinel structure of zinc ferrite. The presence of broad absorption bands at 1650 and 3410 cm^{-1} are the contribution from the vibration of O–H group of adsorbed organic residues and water on the surface of $ZnFe_2O_4$, respectively. In addition, the sharp band at 1384 cm^{-1} clearly demonstrates the presence of nitrate group, which is originally from the usage of metal nitrate salts as the precursors for $ZnFe_2O_4$ preparation. It is clear that the FTIR spectrum of $ZnFe_2O_4$–TiO_2 nanocomposites exhibits the main characteristic peaks of TiO_2 at 455 cm^{-1} and $ZnFe_2O_4$ at 1650 and 3410 cm^{-1}. Moreover, additional peaks at 2924, 2852, 1106 and 1045 cm^{-1} are also observed. The 2924 and 2852 cm^{-1} peaks are the typical symmetric and asymmetric C–H stretching vibrations, respectively, whereas 1106 cm^{-1} is the C–O–H bond and 1045 cm^{-1} can be assigned as the C–O–C bond. Fig. S2 (ESI†) shows the FTIR spectrum of octanol, the solvent used for preparation of $ZnFe_2O_4$–TiO_2. Four major peaks at 2924, 2852, 1106 and 1045 cm^{-1} are clearly observed, which is in good agreement with those of $ZnFe_2O_4$–TiO_2 nanocomposites. This indicates that the functional groups on the surface of $ZnFe_2O_4$–TiO_2 is mainly from the octanol residues.

The thermal property of $ZnFe_2O_4$–TiO_2 nanocomposites was further examined. As shown in Fig. 2c, the TGA curve of ST-01 TiO_2 nanoparticles shows a continuous weight loss from room temperature to 1000 °C in N_2, and a total of 13% weight loss, mainly from the desorption of physically adsorbed water as well as the decomposition of adsorbed organic substances, is observed. Different from the thermal property of commercial TiO_2, three major weight loss regions with a total weight loss of 15% are identified in the decomposition profile of $ZnFe_2O_4$. The weight loss from room temperature to 200 °C corresponds to the evaporation of trapped moisture and the removal of interstitial water molecule, while the decomposition at 200–400 °C is attributed from the thermal-labile organic functional groups onto $ZnFe_2O_4$ surface. The slight decrease in weight loss in the range of 400–1000 °C is due to the decomposition of long-chained organic moieties (oleic acid and oleylamine) on the surface. The TGA curve of $ZnFe_2O_4$–TiO_2 shows a relatively high thermal stability in the initial decomposition temperature range of 25–200 °C. The weight of nanocomposites decrease obviously in the temperature region of 200–450 °C and then follows a slight decrease at 450–800 °C, which is mainly attributed to the decomposition of organic matrix residues on the surface of $ZnFe_2O_4$–TiO_2 nanocomposites during synthesis.

EIS was further performed to investigate the separation and transport processes of photogenerated electron–holes in the photocatalysts. As shown in Fig. 2d, all the Nyquist plots of impedance spectra consist of a semicircle arc and a straight-line portion. The semicircle in high frequency region can be regarded as the characteristics of charge transfer process, while the linear line at low frequency corresponds to the diffusion-controlled step.[39,40] It can be seen that the $ZnFe_2O_4$–TiO_2 nanocomposites has a much smaller arc diameter than those of pure TiO_2 and $ZnFe_2O_4$ nanoparticles, clearly indicating that the combination of p-type $ZnFe_2O_4$ and n-type TiO_2 significantly reduces the charge transfer resistance. The low charge transfer resistance is mainly contributed from the efficient separation of electron–hole pairs, and would result in the high photocatalytic activity of $ZnFe_2O_4$–TiO_2 nanocomposites.

3.2. Effect of light source on photocatalytic activity of $ZnFe_2O_4$–TiO_2

The visible-light-driven photocatalytic activity of $ZnFe_2O_4$–TiO_2 toward BPA degradation was first evaluated by the irradiation of 3 different light sources, 365 UV light, 465 nm visible light and solar simulator. Fig. 3a shows the photodegradation efficiency of 10 mg L^{-1} BPA by $ZnFe_2O_4$–TiO_2 in the presence of different light sources. 35% of the original BPA are removed within 30 min when $ZnFe_2O_4$–TiO_2 is irradiated with 365 nm UV light. Different from the photodegradation behavior under UV light irradiation, a nearly complete photodegradation of BPA is observed when solar simulator is used as the light source. Interestingly, the photocatalytic activity of $ZnFe_2O_4$–TiO_2 can be enhanced under 465 nm visible light irradiation and a nearly complete degradation efficiency of BPA is observed after 20 min of visible light irradiation. The blank control experiments show that the as-prepared $ZnFe_2O_4$ has little photocatalytic activity toward BPA degradation in the presence of different light sources (Fig. S3a, ESI†), presumably due to the rapid hole–electron recombination rate.[24,25] In addition, the photodegradation efficiencies of BPA by pure ST-01 TiO_2 nanoparticles are in the range of 30–46% and follows the order 365 nm UV light > solar light > 465 nm visible light (Fig. S3b, ESI†). Notably, 1 wt% $ZnFe_2O_4$ was physically mixed with TiO_2 and then used for photodegradation of BPA under different light sources irradiation. As shown in Fig. S3c (ESI†), the photodegradation efficiency of BPA by physical mixing of 1 wt% $ZnFe_2O_4$ and TiO_2 under different light sources is in the range of 32–44% after 30 min of irradiation, which is similar to that by pure ST-01 TiO_2 nanoparticles. This result clearly indicates that the formation of heterojunction between $ZnFe_2O_4$ and TiO_2

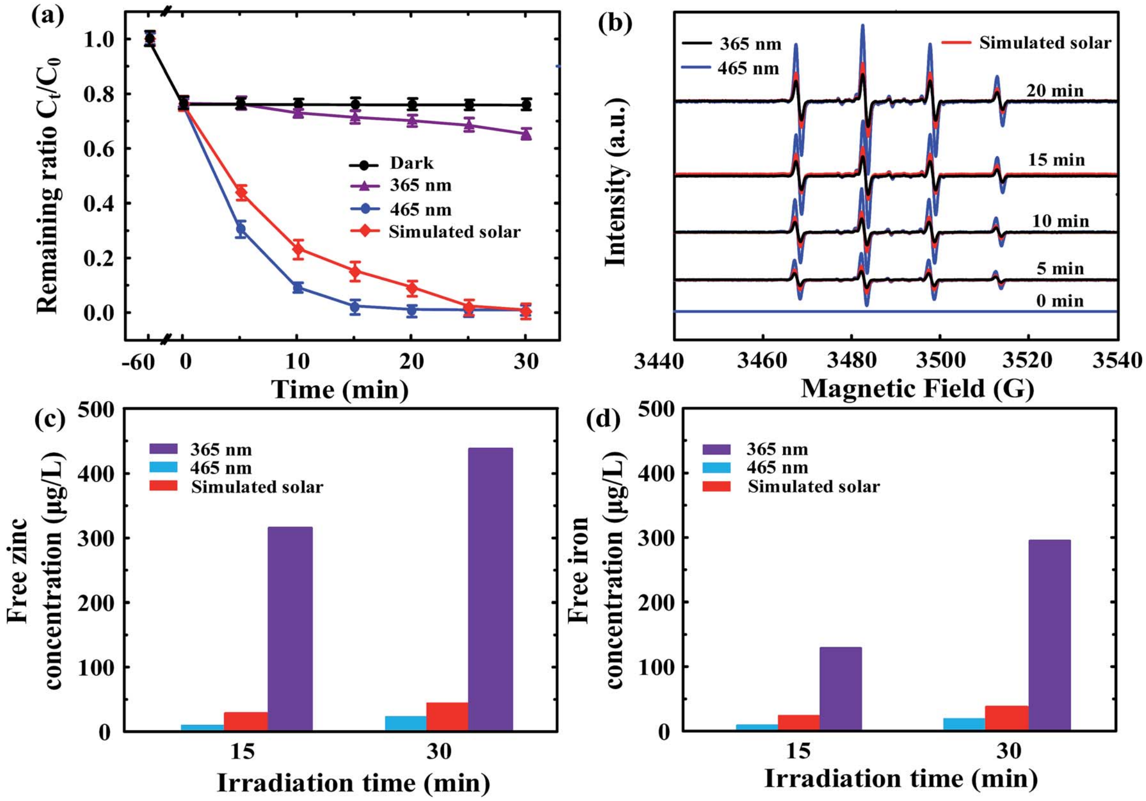

Fig. 3 (a) The photodegradation of 10 mg L^{-1} BPA by $ZnFe_2O_4$–TiO_2 under different light sources irradiation, (b) ESR spectra of DMPO–$^{\bullet}OH$ spin adduct and the aqueous (c) Zn and (d) Fe concentrations in $ZnFe_2O_4$–TiO_2 suspension at various irradiation time intervals by different light sources. The light sources used are 365 nm UV light, 465 nm visible light and solar simulator.

nanoparticles plays a decisive role in enhancing the visible-light-sensitive photocatalytic activity of $ZnFe_2O_4$–TiO_2 heterojunction prepared by hydrothermal method.

To further make sure the photodegradability of BPA by TiO_2 in the presence of different light sources, Degussa P25 TiO_2 was used as the photocatalyst. As shown in Fig. S4 (ESI†), the removal efficiency of BPA by P25 TiO_2 are 93%, 62% and 30% when irradiated with 365 nm UV light, solar simulator and 465 nm visible light, respectively, clearly showing that pure TiO_2 nanoparticles has high photoactivity in the presence of UV light. These results also confirm the superior visible-light-responsive photocatalytic activity of $ZnFe_2O_4$–TiO_2 nanocomposites toward BPA degradation to that under UV light irradiation. It is noteworthy that 10–23% of BPA are adsorbed within 60 min under dark reaction, presumably attributed to the fact that the $ZnFe_2O_4$–TiO_2 nanocomposites are fabricated under non-aqueous solution and the surface contains some trace amounts of organics, which is in good agreement with the FTIR and TGA results shown in Fig. 2b and c.

The photocatalytic degradation of BPA by $ZnFe_2O_4$–TiO_2 follows the pseudo-first-order kinetics and the pseudo-first-order rate constants (k_{obs}) for BPA degradation in the presence of 465 nm visible light, solar simulator and 365 nm UV light are 0.218, 0.141 and 0.0052 min^{-1}, respectively. It is noteworthy that the photocatalytic activity of $ZnFe_2O_4$–TiO_2 under 465 nm visible light irradiation is 42 times higher than that under 365 nm UV light irradiation. Usually short wavelength can provide more energy for photocatalysts to enhance the photodegradation efficiency. Interestingly, the $ZnFe_2O_4$–TiO_2 irradiated with 465 nm visible light in this study has demonstrated the superior photocatalytic activity to that with 365 nm UV light. One of the possible reasons is that 365 nm UV light can trigger the photogenerated hole–electron pairs for both $ZnFe_2O_4$ and TiO_2 and then the hole–electron pairs would undergo the rapid recombination inside the TiO_2 and $ZnFe_2O_4$. Fig. 3b shows the ESR spectra of free radicals produced from BPA solution containing 1 g L^{-1} of $ZnFe_2O_4$–TiO_2 and 4.4 mM DMPO under different light sources irradiation. No ESR signal is produced under the dark reaction. After irradiation with different light sources for 5–20 min, the four-line ESR signals with characteristic 1 : 2 : 2 : 1 quartet of DMPO–OH spin adducts are clearly observed, indicating the production of $^{\bullet}OH$ radicals.[41] In addition, the peak intensity follows the order 465 nm visible light > solar simulator > 365 nm UV light, which means that the $ZnFe_2O_4$–TiO_2 with p–n heterojunction in the presence of visible light can separate e^- and h^+ effectively to accelerate the generation of $^{\bullet}OH$ radicals for photodegradation of BPA. It is noteworthy that the production of hydroxyl radicals increases with the increase in irradiation time and shows a good relationship with the removal efficiency of BPA in the presence of different light sources, clearly indicating that hydroxyl radical is one of the reactive species for BPA photodegradation.

Another plausible reason for the inferior photoactivity of $ZnFe_2O_4$ at 365 nm UV light is the photo-stability of $ZnFe_2O_4$ after irradiation. Fig. 3c and d shows the aqueous Zn and Fe concentrations after irradiation with different light sources at pH 7, respectively. It is clear that the released concentrations of Zn and Fe are only 10–24 and 8–19 $\mu g\ L^{-1}$, respectively, under the irradiation of 465 nm visible light. The aqueous concentrations of Zn and Fe slightly increase to 28–45 and 24–37 $\mu g\ L^{-1}$, respectively, when the light source changes to solar simulator, showing that $ZnFe_2O_4$ is photo-stable under the visible light and solar simulator irradiation. In contrast, the aqueous Zn and Fe concentrations are 315 and 128 $\mu g\ L^{-1}$ after 15 min of UV light irradiation and then increase to 438 and 294 $\mu g\ L^{-1}$, respectively, when the irradiation time prolongs to 30 min. These results clearly indicate the photolabile of $ZnFe_2O_4$ under UV light irradiation. It is noteworthy that the formation of $ZnFe_2O_4$ is a solid reaction between ZnO and Fe_2O_3 and all the light sources can trigger the photo-corrosion of $ZnFe_2O_4$–TiO_2. Since the bandgap of $ZnFe_2O_4$ is only 1.9 eV,[31] the irradiation of UV light generate holes more readily to attack oxygen atoms in Zn–O bond of $ZnFe_2O_4$ $\left(\mathrm{ZnO}+2\mathrm{h}^{+}+n\mathrm{H_2O}\rightarrow\mathrm{Zn(OH)}_n^{(2-n)+}+\frac{1}{2}\mathrm{O_2}+n\mathrm{H}^{+}\right)$,[42] and subsequently results in the increase in photo-corrosion rate of $ZnFe_2O_4$–TiO_2 nanocomposites in comparison with other two light sources. Since the irradiation of both 465 nm visible light and solar simulator can exhibit excellent visible-light-driven photocatalytic activity of $ZnFe_2O_4$–TiO_2 and the k_{obs} for BPA photodegradation under 465 nm visible light irradiation is higher than that in the presence of solar simulator, 465 nm visible light is used as the light source for further experiments.

3.3. Effect of initial BPA concentration on photoactivity of $ZnFe_2O_4$–TiO_2

Fig. 4 shows the photodegradation efficiency and rate of various initial concentrations of BPA by $ZnFe_2O_4$–TiO_2 under 465 nm visible light irradiation at 25 °C and at pH 7. It is evident that the photodegradation efficiency and rate of BPA decreases with the increase in initial BPA concentrations from 5 to 40 $mg\ L^{-1}$. As shown in Fig. 4a, a nearly complete photodegradation of 5 $mg\ L^{-1}$ BPA by $ZnFe_2O_4$–TiO_2 is observed within 15 min of irradiation. However, 30 min of irradiation is need to achieve the same removal efficiency (>99%) when BPA concentration increases to 40 $mg\ L^{-1}$. The photodegradation of BPA at various initial concentrations also follows the pseudo-first-order kinetics and the k_{obs} for BPA photodegradation decreases from 0.295 to 0.096 min^{-1} when the initial BPA concentration increases from 5 to 40 $mg\ L^{-1}$ (inset of Fig. 4a).

Several studies have depicted that the photocatalytic degradation is a surface-mediated reaction and the photocatalytic efficiency and rate is highly dependent on the active sites onto the photocatalyst.[8,31,43,44] Therefore, the Langmuir–Hinshelwood kinetics can be employed to describe the relationship (eqn (1)). Fig. 4b shows the relationship between the initial rate of BPA photodegradation and the initial BPA concentration. It is clear that the initial rate of BPA photodegradation increases rapidly from 0.572 to 1.974 $mg\ L^{-1}\ min^{-1}$ at initial BPA concentration of 5–30 $mg\ L^{-1}$ and then reaches the plateau of 2.051 $mg\ L^{-1}\ min^{-1}$ at 40 $mg\ L^{-1}$ BPA. A good linear relationship between $1/r_0$ and $1/C_R$ with correlation coefficient (r^2) of 0.998 is observed (inset of Fig. 4b). The K_a and k_r values are calculated to be 0.038 $L\ mg^{-1}$ and 3.553 $mg\ L^{-1}\ min^{-1}$, respectively, clearly showing that the photodegradation of BPA by $ZnFe_2O_4$–TiO_2 is a surface-mediated process.

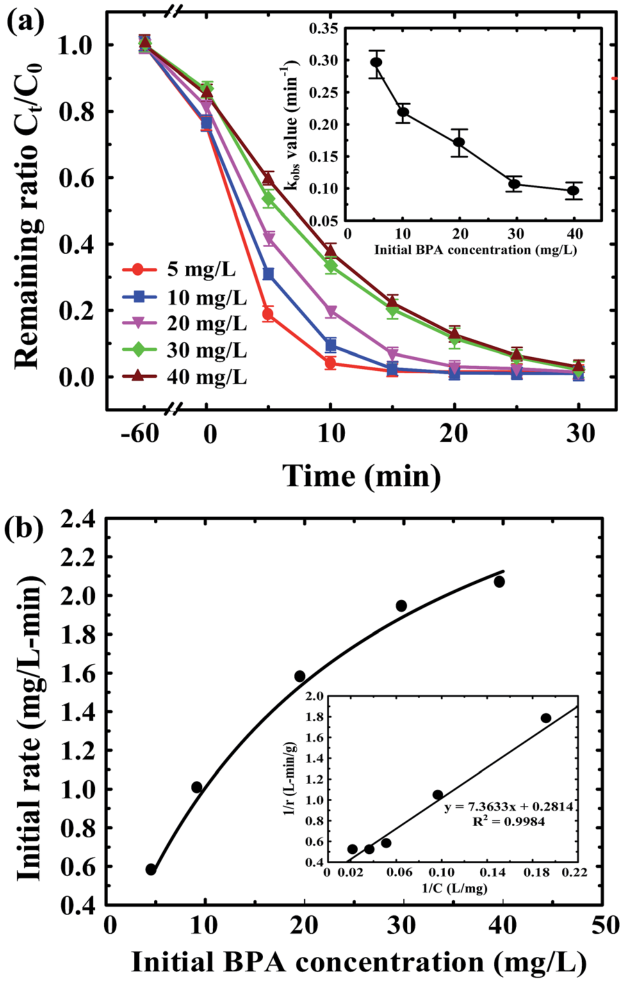

Fig. 4 The (a) photocatalytic degradation of BPA at various initial concentrations and (b) initial rate of BPA as a function of initial BPA concentrations by 1 wt% $ZnFe_2O_4$–TiO_2 under visible light irradiation.

3.4. Stability and reusability of $ZnFe_2O_4$–TiO_2

The reusability is an important factor for evaluation of the possible application of photocatalysts. In this study, the stability and reusability of 1 wt% $ZnFe_2O_4$–TiO_2 nanoparticles were examined by repeated injection of 10 $mg\ L^{-1}$ BPA into the solution at pH 7 under visible light irradiation. Fig. 5a shows the photocatalytic degradation efficiency and rate of BPA by $ZnFe_2O_4$–TiO_2 over 10 repeated cycles of usage. It is apparent that a nearly complete photodegradation of BPA by $ZnFe_2O_4$–TiO_2 can be rapidly achieved within 30 min of visible light irradiation even after 10 cycles of continuous usage. Fig. 5b

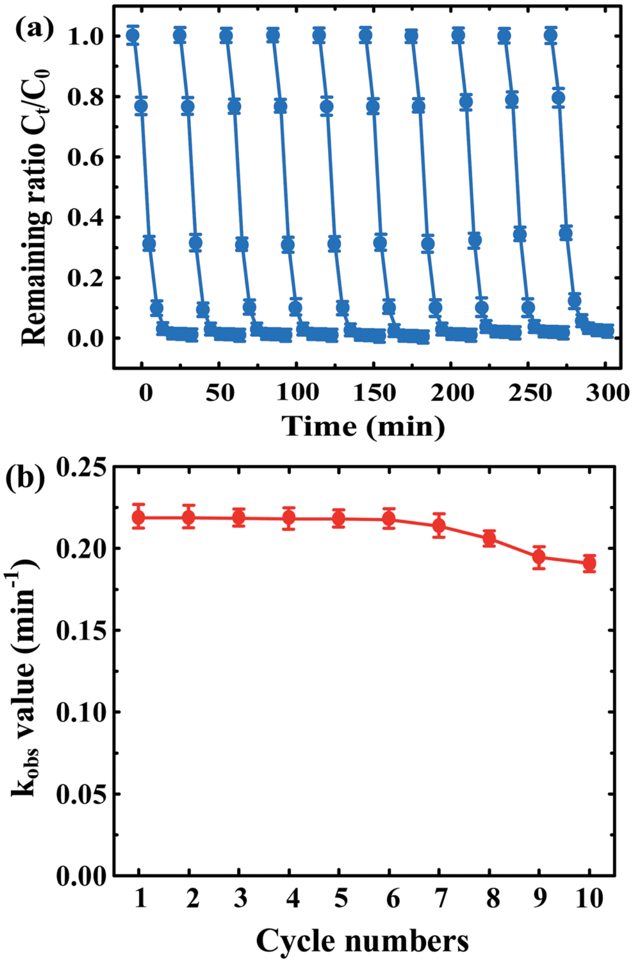

Fig. 5 (a) The recyclability and (b) reaction rate constant of 10 mg L^{-1} BPA by $ZnFe_2O_4$–TiO_2 nanocomposites under 465 nm visible light irradiation at pH 7.

shows the k_{obs} for BPA photodegradation as a function of cycling time. The reaction rate of BPA is almost the same during the first 6 cycles and then decreases slightly from 0.218 min^{-1} at 6th cycle to 0.191 min^{-1} at the 10th cycle, clearly indicating the excellent visible-light-responsive activity and recyclability of $ZnFe_2O_4$–TiO_2 nanocomposites. The slight decrease in k_{obs} is attributed to the accumulation of inter mediates after photocatalytic degradation of BPA and loss of the trace amount of photocatalyst during separation.[44–47] In addition, the released aqueous concentrations of Zn and Fe after 10 cycles are 32 and 21 μg L^{-1}, respectively, which are far lower than the standards of Zn (5 mg L^{-1}) and Fe (0.3 mg L^{-1}) in drinking water. These results indicate that $ZnFe_2O_4$–TiO_2 is an environmentally friendly and stable photocatalyst, which can maintain the highly recyclable photoactivity under visible light irradiation conditions.

3.5. Photocatalytic reaction mechanism of $ZnFe_2O_4$–TiO_2 nanocomposites

To further identify the possible reaction mechanism for BPA photodegradation by $ZnFe_2O_4$–TiO_2, the main oxidative species involving in the photodegradation of BPA are determined through ESR spectra and radical trapping experiments. Fig. 6a shows the ESR spectra of free radicals produced from the visible light irradiation of $ZnFe_2O_4$–TiO_2 nanocomposites in ethanol and aqueous solutions. No ESR signal is produced in both ethanol and aqueous solutions containing DMPO and $ZnFe_2O_4$–TiO_2 in the presence of BPA in the dark. After irradiation of $ZnFe_2O_4$–TiO_2 with visible light in ethanol solution, the six-line ESR spectra are clearly observed, indicating the generation of O-centered radical adducts such as $O_2^{-•}$ and $HO_2^•$. In addition, ethanol serves as the scavenger of $^•OH$ radicals to produce $CH_3CH_2O^•$ radicals and water ($CH_3CH_2OH + {}^•OH \rightarrow CH_3CH_2O^• + H_2O$), and subsequently diminish the ESR signal of $^•OH$ radicals. In contrast, the ESR spectrum of $ZnFe_2O_4$–TiO_2 shows a typical $^•OH$ radical pattern in aqueous solution, which

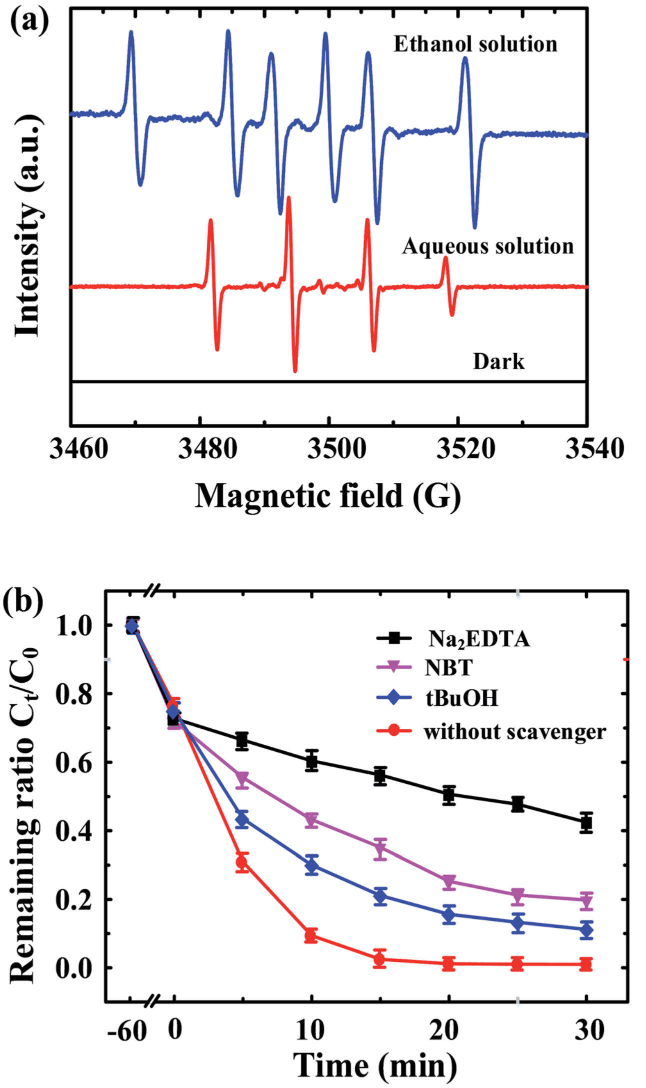

Fig. 6 (a) The ESR spectra of $ZnFe_2O_4$–TiO_2 under visible light irradiation in ethanol and aqueous solutions and (b) the visible-light-driven photocatalytic degradation of BPA by 1 wt% $ZnFe_2O_4$–TiO_2 in the presence of 1 mM various radical scavengers including *tert*-butanol (*t*-BuOH), nitroblue tetrazolium (NBT) and Na_2EDTA.

indicates the reaction of oxygen-containing radicals with water molecules to produce $^{\bullet}OH$ radicals.

For radical trapping experiments, 1 mM *tert*-butanol (*t*-BuOH), nitroblue tetrazolium (NBT) and Na_2EDTA are used as the scavengers for hydroxyl ($^{\bullet}OH$), superoxide anion radical ($O_2^{-\bullet}$) and hole (h^+), respectively. As shown in Fig. 6b, the photocatalytic degradation efficiency of BPA by $ZnFe_2O_4$–TiO_2 decreases after the injection of different scavengers. The photodegradation efficiencies of BPA decrease from >99% in the absence of scavenger to 89, 80 and 57% after 30 min of visible light irradiation when *t*-BuOH, NBT and Na_2EDTA, respectively, are added. In addition, the k_{obs} for BPA photodegradation by $ZnFe_2O_4$–TiO_2 decreases obviously from 0.218 min^{-1} in the absence of scavenger to 0.083 min^{-1} for *t*-BuOH, 0.048 min^{-1} for NBT and 0.017 min^{-1} for Na_2EDTA. It is clear that the degradation efficiency and rate of BPA by $ZnFe_2O_4$–TiO_2 is remarkably restrained after the addition of Na_2EDTA, indicating that the photogenerated holes (h^+) on the surface of $ZnFe_2O_4$–TiO_2 are the predominant reactive species responsible for the photocatalytic degradation of BPA under 465 nm visible light irradiation.

The superoxide anion radicals, produced from the reaction of oxygen with photogenerated electrons, also act as another key factor in the photocatalytic process. It is noteworthy that the photogenerated holes (h^+) in the valence band (VB) of $ZnFe_2O_4$ cannot react with the surface-absorbed H_2O to generate the highly reactive hydroxyl radicals ($^{\bullet}OH$) because of the low VB position (0.38 eV) in comparison with that of water oxidation [$E^0(^{\bullet}OH/OH^-) = 2.38$ V]. Therefore, the generation of hydroxyl radicals in the heterogeneous photocatalytic system under visible light irradiation is mainly produced from the chain reactions of superoxide anion radicals with proton and/or photogenerated electrons. The above mentioned results clearly indicate that the direct hole oxidation and the oxidation from the oxygen-containing radicals such as $^{\bullet}OH$ and $O_2^{-\bullet}$ are the major reaction mechanisms for the photocatalytic degradation of BPA under visible light irradiation conditions. The excellent photocatalytic activity of $ZnFe_2O_4$–TiO_2 toward BPA degradation is mainly contributed from the high efficiency of electron–hole separation induced by the p–n heterojunction of $ZnFe_2O_4$–TiO_2 nanocomposites. Fig. 7 shows the possible visible-light-driven reaction mechanisms for BPA photodegradation by $ZnFe_2O_4$–TiO_2 nanocomposites in the presence of 465 nm visible light. Electrons in the VB of $ZnFe_2O_4$ can be photo-excited to the conduction band (CB) to produce the electron–hole pairs after the irradiation of visible light (pathway 1). Since the redox potential position of CB of $ZnFe_2O_4$ at −1.54 eV is higher than that of anatase TiO_2 (−0.29 eV), the excited electrons in $ZnFe_2O_4$ can be easily transferred across the interface of nanocomposites to the CB of anatase TiO_2, and leave holes in the VB of $ZnFe_2O_4$ (pathway 2). Therefore, the coupling of p-type $ZnFe_2O_4$ and n-type TiO_2 can effectively reduce the recombination rate of electrons and holes, and subsequently decreases the internal resistance as well as enhances the interfacial charge transfer efficiency, which can be seen in the EIS spectra (Fig. 2d). Therefore, the photogenerated holes (h^+) in the VB of $ZnFe_2O_4$ can directly photodegrade BPA under the irradiation of 465 nm visible light (pathway 3). In

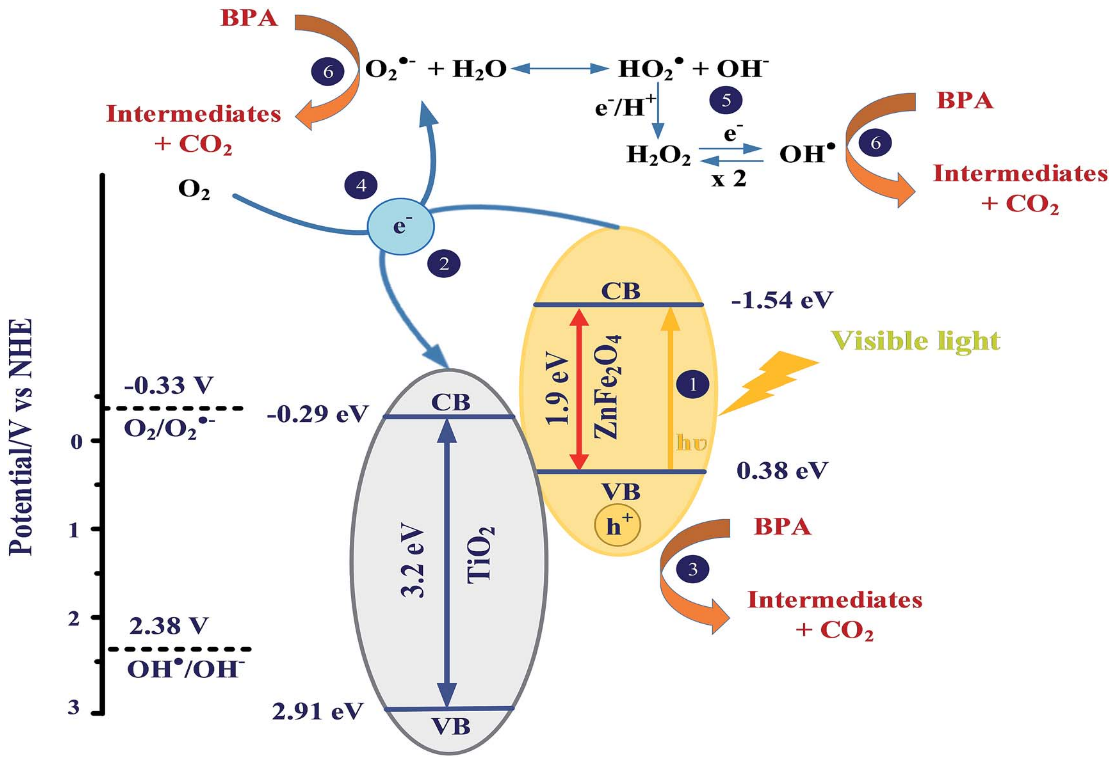

Fig. 7 Schematic illustration of visible-light-driven photodegradation of BPA by $ZnFe_2O_4$–TiO_2 photocatalysts under visible light irradiation.

addition, the reduction potential of electrons in the VB of TiO_2 at pH 7 is −0.29 V, which can provide sufficient reducing power to react with oxygen to generate superoxide anion ($O_2^{-\bullet}$) and peroxyl ($HO_2^{\bullet}$) radicals [$E^0(O_2/O_2^{-\bullet}) = -0.33$ V and $E^0(O_2/HO_2^{\bullet}) = -0.05$ V] (pathways 4 and 5). The produced oxygen-containing radicals ($O_2^{-\bullet}$ and $HO_2^{\bullet}$) can further react with electrons and protons to produce hydroxyl radicals ($^{\bullet}OH$). Since the produced hydroxyl radicals can be prolonging to more than 20 min (Fig. 3b), the photocatalytic degradation efficiency and rate of BPA can be significantly enhanced under visible light irradiation (pathway 6).

4. Conclusions

In this study, we have, for the first time, demonstrated the excellent visible-light-driven photocatalytic activity of $ZnFe_2O_4$–TiO_2 nanocomposites toward BPA degradation under 465 nm visible light irradiation. The intimate heterojunction interface between p-type $ZnFe_2O_4$ and n-type TiO_2 can facilitate the charge transfer more readily, resulting in the reduction of recombination efficiency of electron–hole pairs as well as the enhancement of visible-light-responsive photocatalytic activity of $ZnFe_2O_4$–TiO_2 nanocomposites. The photocatalytic activity of $ZnFe_2O_4$–TiO_2 under 465 nm visible light irradiation is 42 times higher than that under 365 nm UV light irradiation. In addition, the $ZnFe_2O_4$–TiO_2 nanocomposites can retain their photocatalytic efficiency for at least 10 cycles of reaction with stable photodegradation rate constants under visible light irradiation. The radical trapping experiments indicates that photogenerated holes as well as oxygen-containing radicals are the predominant reactive species responsible for the photodegradation of BPA in the $ZnFe_2O_4$–TiO_2 system. In addition, $ZnFe_2O_4$–TiO_2 still shows excellent photocatalytic activity toward BPA photodegradation under solar simulator irradiation, indicating the possible photocatalytic application of $ZnFe_2O_4$–TiO_2 in natural aquatic environments. Results obtained in this study clearly demonstrate that $ZnFe_2O_4$–TiO_2 is a reliable green photocatalyst with superior photocatalytic activity toward BPA under visible light irradiation, which can open an avenue to fabricate p–n heterojunction photocatalysts approach with great potential applications of utilizing visible light for removal of recalcitrant and emerging pollutants, water splitting and energy conversion.

Conflicts of interest

There are no conflicts to declare.

Acknowledgements

The authors thank the Ministry of Science and Technology (MOST), Taiwan for financial support under grant No. MOST 104-2221-E-009-020-MY3 and 105-2113-M-009-023-MY3.

Notes and references

1 M. Dahl, Y. D. Liu and Y. D. Yin, *Chem. Rev.*, 2014, **114**, 9853–9889.
2 K. Yan and G. S. Wu, *ACS Sustainable Chem. Eng.*, 2015, **3**, 779–791.
3 G. K. Mor, O. K. Varghese, M. Paulose, K. Shankar and C. A. Grimes, *Sol. Energy Mater. Sol. Cells*, 2006, **90**, 2011–2075.
4 R. A. Doong, S. M. Chang and C. W. Tsai, *Appl. Catal., B*, 2013, **129**, 48–55.
5 G. M. Wang, H. Y. Wang, Y. C. Ling, Y. C. Tang, X. Y. Yang, R. C. Fitzmorris, C. C. Wang, J. Z. Zhang and Y. Li, *Nano Lett.*, 2011, **11**, 3026–3033.
6 C. L. Li, J. A. Yuan, B. Y. Han, L. Jiang and W. F. Shangguan, *Int. J. Hydrogen Energy*, 2010, **35**, 7073–7079.
7 S. W. Liu, J. G. Yu and M. Jaroniec, *J. Am. Chem. Soc.*, 2010, **132**, 11914–11916.
8 R. A. Doong, C. W. Tsai and C. I. Liao, *Sep. Purif. Technol.*, 2012, **91**, 81–88.
9 M. O. Ojemay, O. O. Okoh and A. I. Okoh, *J. Nanomater.*, 2017, **2017**, 1–10.
10 H. Z. Li, L. Zhang, Z. B. Sun, Y. Liu, B. Yang and S. Q. Yan, *RSC Adv.*, 2015, **5**, 31787–31797.
11 N. Nasrallah, M. Kebir, Z. Koudri and M. Trari, *J. Hazard. Mater.*, 2011, **185**, 1398–1404.
12 J. Rawat, S. Rana, R. Srivastava and R. D. K. Misra, *Mater. Sci. Eng., C*, 2007, **27**, 540–545.
13 N. M. Mahmoodi, *Desalination*, 2011, **279**, 332–337.
14 Y. J. Yao, Y. M. Cai, F. Lu, J. C. Qin, F. Y. Wei, C. Xu and S. B. Wang, *Ind. Eng. Chem. Res.*, 2014, **53**, 17294–17302.
15 L. L. Zou, Q. J. Wang, X. Q. Shen, Z. Wang, M. X. Jing and Z. Luo, *Appl. Surf. Sci.*, 2015, **332**, 674–681.
16 M. H. Su, C. He, V. K. Sharma, M. Abou Asi, D. Xia, X. Z. Li, H. Q. Deng and Y. Xiong, *J. Hazard. Mater.*, 2012, **211**, 95–103.
17 K. N. Harish, H. S. B. Naik, P. N. P. Kumar and R. Viswanath, *ACS Sustainable Chem. Eng.*, 2013, **1**, 1143–1153.
18 R. Dom, R. Subasri, K. Radha and P. H. Borse, *Solid State Commun.*, 2011, **151**, 470–473.
19 F. Zhang, X. Y. Li, Q. D. Zhao and D. K. Zhang, *ACS Sustainable Chem. Eng.*, 2016, **4**, 4554–4562.
20 A. Sheikh, A. Yengantiwar, M. Deo, S. Kelkar and S. Ogale, *Small*, 2013, **9**, 2091–2096.
21 K. J. McDonald and K. S. Choi, *Chem. Mater.*, 2011, **23**, 4863–4869.
22 J. Hu, Y. H. Xie, X. F. Zhou and J. Y. Yang, *J. Alloys Compd.*, 2016, **676**, 320–325.
23 C. Cai, Z. Y. Zhang, J. Liu, N. Shan, H. Zhang and D. D. Dionysiou, *Appl. Catal., B*, 2016, **182**, 456–468.
24 W. Q. Zhang, M. Wang, W. J. Zhao and B. Q. Wang, *Dalton Trans.*, 2013, **42**, 15464–15474.
25 T. P. Xie, L. J. Xu, C. L. Liu and Y. Wang, *Appl. Surf. Sci.*, 2013, **273**, 684–691.
26 X. Zhu, F. Zhang, M. Wang, J. Ding, S. Sun, J. Bao and C. Gao, *Appl. Surf. Sci.*, 2014, **319**, 83–89.
27 L. Sun, R. Shao, L. Q. Tang and Z. F. Chen, *J. Alloys Compd.*, 2013, **564**, 55–62.
28 Y. Fu and X. Wang, *Ind. Eng. Chem. Res.*, 2011, **50**, 7210–7218.
29 M. K. Nowotny, P. Bogdanoff, T. Dittrich, S. Fiechter, A. Fujishima and H. Tributsch, *Mater. Lett.*, 2010, **64**, 928–930.

30 L. Kong, Z. Jiang, T. Xiao, L. Lu, M. O. Jones and P. P. Edwards, *Chem. Commun.*, 2011, **47**, 5512–5514.

31 T. B. Nguyen and R. A. Doong, *RSC Adv.*, 2016, **6**, 103428–103437.

32 T. Deblonde, C. Cossu-Leguille and P. Hartemann, *Int. J. Hyg. Environ. Health*, 2011, **214**, 442–448.

33 Y. Q. Huang, C. K. C. Wong, J. S. Zheng, H. Bouwman, R. Barra, B. Wahlstrom, L. Neretin and M. H. Wong, *Environ. Int.*, 2012, **42**, 91–99.

34 L. N. Vandenberg, R. Hauser, M. Marcus, N. Olea and W. V. Welshons, *Reprod. Toxicol.*, 2007, **24**, 139–177.

35 V. K. Sharma, G. A. K. Anquandah, R. A. Yngard, H. Kim, J. Fekete, K. Bouzek, A. K. Ray and D. Golovko, *J. Environ. Sci. Health, Part A: Toxic/Hazard. Subst. Environ. Eng.*, 2009, **44**, 423–442.

36 J. K. Du, J. G. Bao, Y. Liu, H. B. Ling, H. Zheng, S. H. Kim and D. D. Dionysiou, *J. Hazard. Mater.*, 2016, **320**, 150–159.

37 X. J. He, W. G. Aker, M. Pelaez, Y. F. Lin, D. D. Dionysiou and H. M. Hwang, *J. Photochem. Photobiol., A*, 2016, **314**, 81–92.

38 L. B. Hoch, P. Szymanski, K. K. Ghuman, L. He, K. Liao, Q. Qiao, L. M. Reyes, Y. M. Zhu, M. A. El-Sayed, C. V. Singh and G. A. Ozin, *Proc. Natl. Acad. Sci. U. S. A.*, 2016, **113**, 8011–8020.

39 X. L. He, Y. Y. Cai, H. M. Zhang and C. H. Liang, *J. Mater. Chem.*, 2011, **21**, 475–480.

40 M. Y. Wang, L. Sun, J. H. Cai, P. Huang, Y. F. Su and C. J. Lin, *J. Mater. Chem. A*, 2013, **1**, 12082–12087.

41 S. M. Chang, P. H. Lo and C. T. Chang, *Appl. Catal., B*, 2009, **91**, 619–627.

42 S. G. Kumar and K. Rao, *RSC Adv.*, 2015, **5**, 3306–3351.

43 M. Chaudhary, S. M. Chang, R. A. Doong and H. M. Tsai, *J. Phys. Chem. C*, 2016, **120**, 21381–21389.

44 L. F. Chiang and R. A. Doong, *Sep. Purif. Technol.*, 2015, **156**, 1003–1010.

45 L. L. Costa and A. G. S. Prado, *J. Photochem. Photobiol., A*, 2009, **201**, 45–49.

46 K. Sorathiya, B. Mishra, A. Kalarikkal, K. P. Reddy, C. S. Gopinath and D. Khushalani, *Sci. Rep.*, 2016, **6**, 35075–35084.

47 R. A. Doong and C. W. Tsai, *J. Taiwan Inst. Chem. Eng.*, 2015, **57**, 69–76.